

In the format provided by the authors and unedited.

Time- and spatially-resolved magnetization dynamics driven by spin-orbit torques

Manuel Baumgartner, Kevin Garello, Johannes Mendil, Can Onur Avci,
Eva Grimaldi, Christoph Murer, Junxiao Feng, Mihai Gabureac, Christian Stamm,
Yves Acremann, Simone Finizio, Sebastian Wintz, Jörg Raabe, Pietro Gambardella

CONTENTS

SI 1. Magnetic characterization and all-electrical pulsed switching measurements	2
SI 2. Harmonic Hall voltage measurements of the spin-orbit torques	3
SI 3. Dependence of the switching speed on the external field B_x	4
SI 4. Micromagnetic simulations of the switching speed as a function of current	5
SI 5. Macrospin model of magnetization reversal at different edge positions	6
SI 6. Effect of the Oersted field	7
SI 7. Switching of defective dots	8
SI 8. Comparison between filtered and raw data	10
References	11

SI 1. MAGNETIC CHARACTERIZATION AND ALL-ELECTRICAL PULSED SWITCHING MEASUREMENTS

Figure S1a shows an atomic force microscope image of a 500 nm wide Co dot on top of a Pt Hall cross deposited on a 200 nm thick Si_3N_4 membrane. The Co dot is 1 nm thick, capped by 2 nm of oxidized Al, and the Pt line is 5 nm thick. This type of samples are replicas of those employed for the scanning transmission x-ray microscopy (STXM) measurements, which we used to characterize the magnetic properties and to perform all-electrical pulsed switching experiments by probing the anomalous Hall effect^{S1}. Figure S1b shows the Hall resistance $R_H = R_{AHE} \cos \theta = R_{AHE} M_z$ measured as a function of the external field B_{ext} applied out-of-plane ($\theta_B = 0^\circ$) and nearly in-plane ($\theta_B = 84^\circ$). Here, θ and θ_B are the polar angles of the magnetization and applied field, respectively, and R_{AHE} is the anomalous Hall coefficient. The square loop measured at $\theta_B = 0^\circ$ shows that the dots have strong perpendicular magnetic anisotropy, with an effective anisotropy field given by $B_K = B_{ext}(\sin \theta_B / \sin \theta - \cos \theta_B / \cos \theta) \approx 660$ mT.

Figure S1c shows pulsed switching measurements as a function of the pulse voltage amplitude U_p (1 V corresponds to $j_p = 8.4 \cdot 10^8$ A/cm² in the Pt line) for different pulse widths τ_p and external fields applied at an angle $\theta_B = 89^\circ$, almost parallel to the current line. Each point represents the difference of the Hall resistance measured after and before the pulse averaged over 200 switching attempts starting from a fully saturated magnetization state. We observe reliable switching at pulse voltages and widths comparable to those used for the STXM measurements, the main difference being that the U_p values in the Hall measurements are about 20 % larger compared to the x-ray measurements due to the dispersion of the current in the Hall cross. In agreement with previous studies^{S1}, we find that the threshold pulse amplitude to achieve switching decreases with increasing pulse width and bias field.

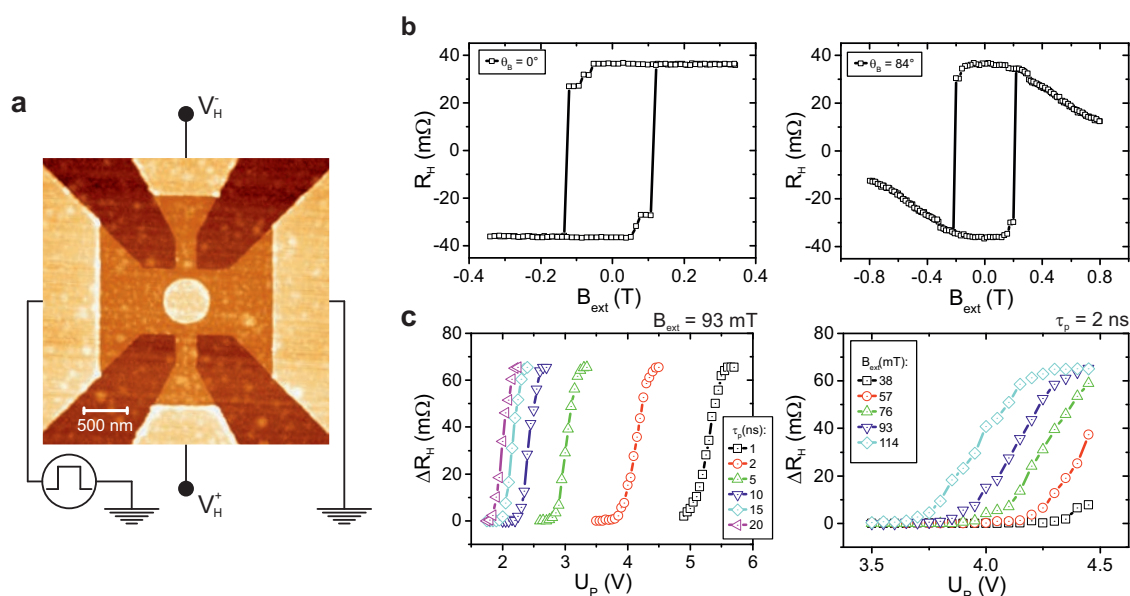


FIG. S1. Magnetic characterization and all-electrical pulsed switching measurements. **a**, Atomic force microscopy image showing a 500 nm Co dot on a 750 nm wide Pt Hall cross grown on a Si_3N_4 membrane. **b**, R_H measured as a function of external field applied out-of-plane (left panel, $\theta_B = 0^\circ$) and nearly in-plane (right panel, $\theta_B = 84^\circ$). **c**, Pulsed magnetization switching measurements as a function of pulse length (left panel) and in-plane bias field (right panel). In both cases the bias field is applied at an angle $\theta_B = 89^\circ$ along the current line.

SI 2. HARMONIC HALL VOLTAGE MEASUREMENTS OF THE SPIN-ORBIT TORQUES

In order to determine the spin-orbit torques (SOTs) and the effective perpendicular anisotropy field in our structures, we performed adiabatic harmonic Hall voltage measurements^{S2,S3} using an ac current of frequency $\omega = 2\pi \cdot 10$ Hz and a current density of $j = 10^7$ A/cm². The sample is a $5\ \mu\text{m}$ wide Hall bar which has been deposited on Si₃N₄ at the same time as the Co dots used for the time-resolved switching experiments described in the main text. The injection of the ac current into the Pt/Co bilayers generates a Hall voltage perpendicular to the current direction, which depends on the orientation of the magnetization due to the anomalous and planar Hall effects. The Hall resistance $R_H = V_H/I = R_H^\omega + R_H^{2\omega}$ includes a first and a second harmonic component. The first harmonic component, shown in the top panels of Fig. S3, is equivalent to the dc Hall resistance, which depends on the equilibrium position of the magnetization as

$$R_H^\omega = R_{AHE} \cos \theta + R_{PHE} \sin^2 \theta \sin(2\varphi), \quad (\text{S1})$$

where R_{PHE} is the planar Hall coefficient and φ the azimuthal angle describing the in-plane orientation of the magnetization relative to the x -axis (see Fig. S2). The second harmonic signal, which is proportional to the current, depends on the SOT-induced reorientation of the magnetization about the equilibrium position as well as on magnetothermal effects scaling with I^2 . The general form of $R_H^{2\omega}$ is given by^{S2,S4}

$$R_H^{2\omega} = [R_{AHE} - 2R_{PHE} \cos \theta \sin(2\varphi)] \frac{d \cos \theta}{dB_{ext}} \frac{B_\theta^I}{\sin(\theta_B - \theta)} + R_{PHE} \sin^2 \theta \frac{2 \cos(2\varphi)}{B_{ext} \sin \theta_B} B_\varphi^I + R_{\nabla T}^{2\omega}, \quad (\text{S2})$$

where B_θ^I and B_φ^I are the polar and azimuthal components of the total current-induced field $\mathbf{B}^I = \mathbf{B}^{DL} + \mathbf{B}^{FL} + \mathbf{B}^{Oe}$. By performing three independent measurements of R_H^ω and $R_H^{2\omega}$ at different angles (for instance at $\varphi_B = 0^\circ, 45^\circ, 90^\circ$, as shown in Fig. S3) with a fixed θ_B , these components can be directly linked to the SOTs expressed in spherical coordinates:

$$\mathbf{B}^{FL} = B_\theta^{FL} \cos \theta \sin \varphi \mathbf{e}_\theta + B_\varphi^{FL} \cos \varphi \mathbf{e}_\varphi, \quad (\text{S3})$$

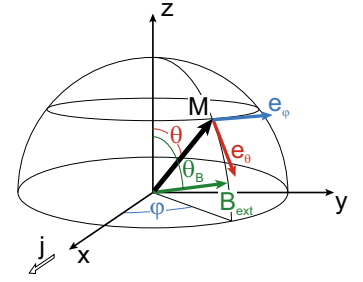


FIG. S2. Coordinate scheme.

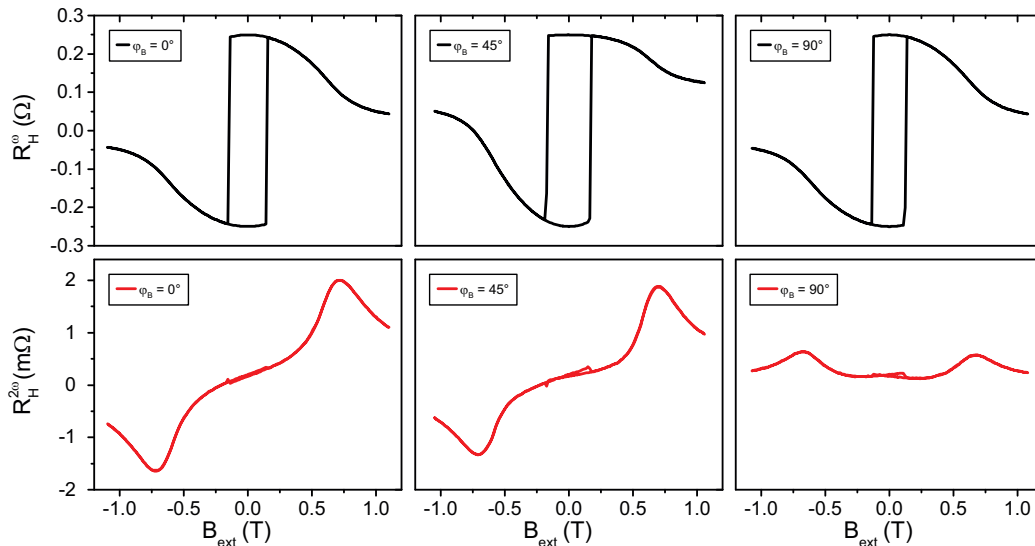


FIG. S3. **Harmonic Hall voltage measurements of the SOTs.** Upper row: First harmonic Hall resistance signals obtained for $\varphi_B = 0^\circ$, $\varphi_B = 45^\circ$ and $\varphi_B = 90^\circ$ at constant $\theta_B = 86^\circ$. Lower row: Corresponding second harmonic signal.

$$\mathbf{B}^{DL} = B_{\theta}^{DL} \cos \varphi \mathbf{e}_{\theta} - B_{\varphi}^{DL} \cos \theta \sin \varphi \mathbf{e}_{\varphi}, \quad (\text{S4})$$

where \mathbf{e}_{φ} and \mathbf{e}_{θ} are the azimuthal and polar unit vectors. The last term in Eq. (S2) is the magnetothermal Hall resistance, which is mainly due to the anomalous Nernst effect induced by Joule heating. This term must be taken into account for accurate SOT quantification. The second harmonic components due to $R_{\nabla T}^{2\omega}$ and the current-induced fields are separated by analyzing the dependence of $R_H^{2\omega}$ on B_{ext} during a field scan with $\theta_B = 90^\circ$ and $\varphi_B = 45^\circ$. As the magnetization saturates in the sample plane at high fields, the susceptibility to the SOT decreases and $R_H^{2\omega} \rightarrow R_{\nabla T}^{2\omega}$. Plotting $R_H^{2\omega}$ as a function of $1/(B_{ext} - B_K)$ allows us to deduce $R_{\nabla T}^{2\omega}$ from the intercept of the coordinate axis^{S4}. In the present case, accounting for $R_{\nabla T}^{2\omega}$ leads to a reduction of the SOTs of about 20 % and 15 % for the field-like (FL) and damping-like (DL) torque, respectively, relative to the values derived from the as-measured $R_H^{2\omega}$. Following this procedure we find that $B^{DL} = 18 \text{ mT}$, and $B^{FL} = B_0^{FL, Oe} + B_2^{FL} \sin^2 \theta$, where $B_0^{FL, Oe} = 10.2 \text{ mT}$ and $B_2^{FL} = 18 \text{ mT}$ for a current density of 10^8 A/cm^2 . The Oersted field contribution is evaluated in Sect. SI 6.

SI 3. DEPENDENCE OF THE SWITCHING SPEED ON THE EXTERNAL FIELD B_x

Figure S4a shows the x-ray magnetic circular dichroism (XMCD) time traces of a Co dot during the injection of 2 ns long current pulses of amplitudes $U_p = -3.35 \text{ V}$ and 3.42 V at different values of the applied field B_x . In the following, we will limit the discussion to negative fields but emphasize that the same arguments are consistent with positive bias fields. We find that B_x has an influence on the reversal speed, namely that switching occurs faster at high field values. This is shown in Fig. S4b where the average slope of the XMCD time traces during the reversal is plotted against B_x . With increasing B_x , M_z decreases while $|M_x|$ increases on one side of the dot, which favours

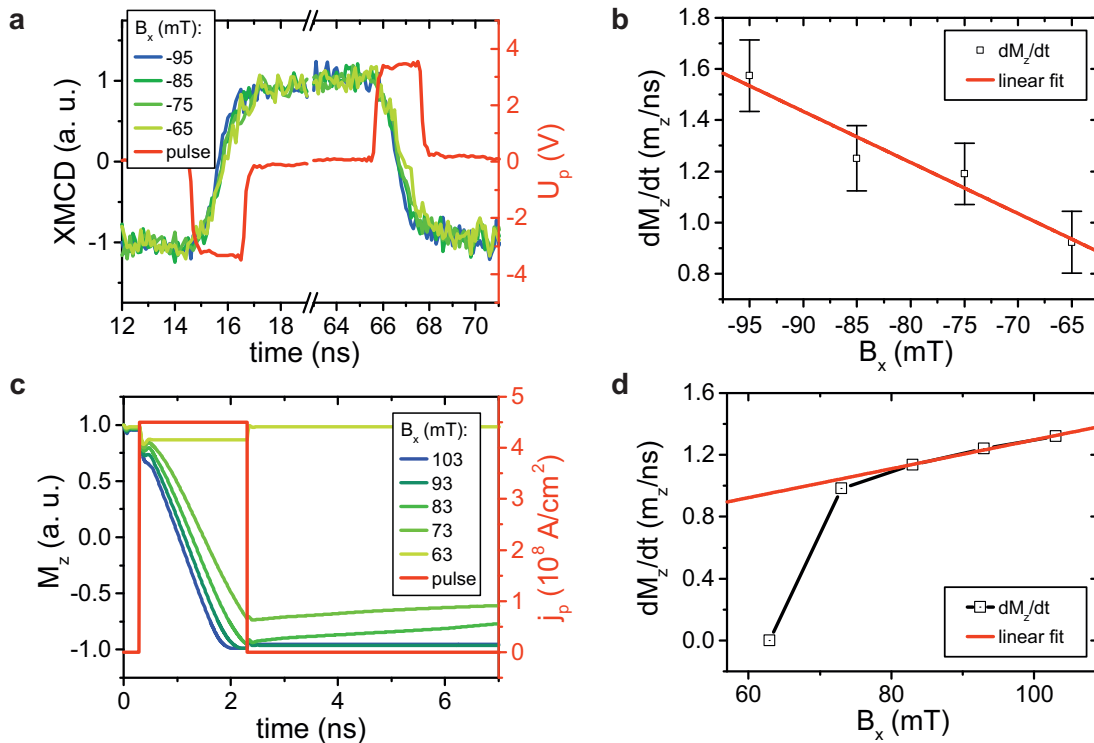


FIG. S4. **Effect of the external in-plane field on the switching speed.** **a**, Measured XMCD time traces as a function of in-plane field B_x . **b**, Average slope of the rising and falling edges during the reversal plotted as function of B_x . **c**, Simulated time traces of M_z as a function of B_x . The slow dynamics after the current pulse is due to the DW reorientation after incomplete magnetization reversal. **d**, Reversal rate $\frac{dM_z}{dt}$ evaluated for the traces shown in c during the current pulse.

magnetization reversal.

Our findings are supported by micromagnetic simulations (see Methods Section) in which we analyze the influence of B_x on the reversal speed. Figure S4c shows the simulated time traces of M_z following the injection of a current pulse of amplitude $j_p = 4.5 \cdot 10^8 \text{ A/cm}^2$ for different values of B_x . The simulations show that there is a threshold bias field $63 \text{ mT} < B_x < 73 \text{ mT}$ below which reversal does not take place. Above this field, the domain wall (DW) velocity increases with B_x as the magnetization tilts more towards the sample plane and the energy barrier for DW propagation reduces, in agreement with the experiment. We further note that the experimental threshold field can be significantly lower compared to the simulations owing to Joule heating, which assists the nucleation of reversed domains.

SI 4. MICROMAGNETIC SIMULATIONS OF THE SWITCHING SPEED AS A FUNCTION OF CURRENT

Micromagnetic simulations performed as a function of j_p show that complete reversal of the dot is achieved faster for larger current densities (Fig. S5a), in agreement with experimental observations. The simulations also evidence an initial tilting motion of the magnetization that precedes the nucleation of a reversed domain at the dot edge. This motion gives rise to a semi-precessional local minimum in the simulated time trace of M_z (inset of Fig. S5b), which can be used to define an effective nucleation time t_N^* . This time decreases with increasing j_p , albeit weakly (Fig. S5b). In theory, such a t_N^* can become a limiting factor for the switching speed of dots of very small size. In practice, however, we do not observe evidence of a distinct nucleation phase within the temporal resolution and sensitivity of our measurements. The question remains open if such a phase exists and can be experimentally resolved. Finally, we note that micromagnetic simulations performed as a function of pulse length at constant current density show that the switched dot area is roughly proportional to the pulse duration for pulses shorter than the time required to achieve full switching, as shown in Fig. S5c.

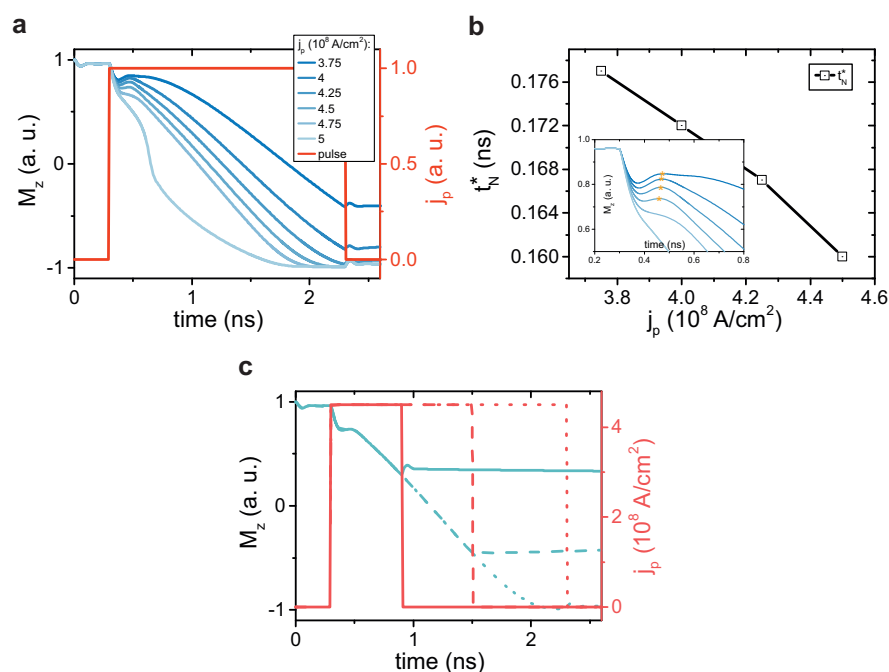


FIG. S5. **Simulations of magnetization reversal as a function of current amplitude and pulse length.** **a**, Simulated time traces of M_z as a function of j_p . **b**, Effective nucleation time t_N^* defined by the duration of the initial tilt motion of the magnetization. Inset: Detail of the traces shown in **a**. The position of the asterisks defines t_N^* . **c**, Simulated time traces of M_z as a function of pulses of length 0.6, 1.2, and 2 ns for $j_p = 4.5 \cdot 10^8 \text{ A/cm}^2$.

SI 5. MACROSPIN MODEL OF MAGNETIZATION REVERSAL AT DIFFERENT EDGE POSITIONS

We provide a simplified and intuitive model of the edge nucleation by simulating the reversal process of four non-interacting single spins located at positions (1) - (4) around the Co dot, as illustrated in Fig. S6a. The Dzyaloshinskii-Moriya interaction (DMI) is included as an effective field by considering the DMI-energy

$$E_{DMI} = \mathbf{D} \cdot (\mathbf{M}_i \times \mathbf{S}), \quad (\text{S5})$$

where \mathbf{M}_i is the magnetization vector of the spin at position (i), \mathbf{S} represents a fictitious central spin of fixed orientation and \mathbf{D} is the DMI-coupling vector. \mathbf{D} lies in the sample plane and is perpendicular to the vector connecting the spins \mathbf{M}_i and \mathbf{S} . It can thus be parametrized by an angle φ_i as $\mathbf{D} = D(\sin \varphi_i, -\cos \varphi_i, 0)$. We then make use of the general relation $\mathbf{B}_{DMI} = -\nabla_{\mathbf{M}} E_{DMI}$ to express the DMI-energy as an effective field

$$\mathbf{B}_{DMI,i} = \text{sgn}(S_z) 2D \begin{pmatrix} \cos \varphi_i \\ \sin \varphi_i \\ 0 \end{pmatrix}. \quad (\text{S6})$$

Finally, we perform a time-integral of the Landau-Lifshitz Gilbert equation to separately model the evolution of the magnetization at points (1) - (4) under the action of $B_{DMI,i}$, $B_x = 100$ mT, effective anisotropy field $B_K = 657$ mT, and the DL and FL torques measured in Section SI 2. We choose the DMI-coupling strength D such that it induces a spin canting at the sample edge similar to that reported in Ref. S5. The canting angle at positions (1) and (2) under a positive bias field of $B_x = 100$ mT is $\approx 18^\circ$ for $D = 60$ mT, whereas it is $\approx 8^\circ$ at positions (3) and (4). For brevity, we limit the discussion to $B_x > 0$ and positive current pulses, as indicated in Fig. S6a.

We consider first the case $S_z > 0$, which represents the dot in the up-state. For a given current, the simulated time traces of the magnetization at positions (1) - (4), reported in Fig. S6b, show that only the spin located at position (1) reverses, whereas, by inverting the sign of B^{FL} and keeping B^{DL} constant, only the spin at position (2) reverses. This behavior is in agreement with the nucleation point observed experimentally (Fig. 3b (II)). Inverting the sign of the central spin, such that $S_z < 0$, changes the direction of the effective DMI-field and makes position (3) equivalent to position (1) in the former case ($S_z > 0$). The effect of the FL torque at different positions can be simply rationalized

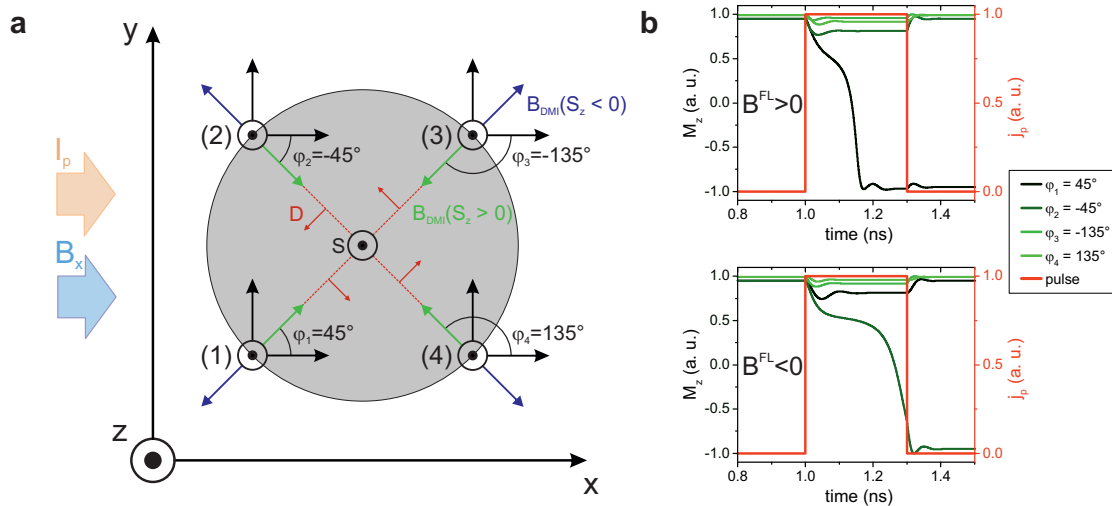


FIG. S6. **Macrospin model of edge magnetization reversal.** **a**, Schematic representation of four non-interacting spins located at distinct positions around the dot. The DMI is taken into account as an effective in-plane field, the sign of which depends on the orientation of the fictitious central spin. **b**, z -component of the four macrospins during the application of a current pulse for $B^{FL} > 0$ (upper panel, corresponding to the experimental situation) and $B^{FL} < 0$ (lower panel).

by considering the θ -component of the field B^{FL} :

$$B_{\theta}^{FL} = \mathbf{B}^{FL} \cdot \mathbf{e}_{\theta} = \begin{pmatrix} 0 \\ B^{FL} \\ 0 \end{pmatrix} \cdot \begin{pmatrix} \cos \theta \cos \varphi_i \\ \cos \theta \sin \varphi_i \\ -\sin \theta \end{pmatrix} = B^{FL} \cos \theta \sin \varphi_i, \quad (\text{S7})$$

where we see that B_{θ}^{FL} depends on φ_i and points towards the xy -plane at position (1) and in the opposite direction at position (2), thus favoring the reversal of spin (1) relative to (2).

SI 6. EFFECT OF THE OERSTED FIELD

The current flowing in the Pt line produces an Oersted field with y - and z -components given by^{S6}

$$B_y^{Oe} = -\frac{I}{wd} (U_y^+ - D_y^+ + U_y^- - D_y^-) \cdot 10^{-7}, \quad B_z^{Oe} = -\frac{I}{wd} (U_z^+ - D_z^+ - U_z^- + D_z^-) \cdot 10^{-7}, \quad (\text{S8})$$

where the field is given in units of Tesla, I is the current in Ampères, w is the width of the Pt line and d its thickness, respectively, in metres. The coefficients are defined as follows:

$$U_y^{\pm} = 2(z+d) \arctan \left[\frac{w/2 \pm y}{z+d} \right] + (w/2 \pm y) \ln \left[(w/2 \pm y)^2 + (z+d)^2 \right], \quad (\text{S9})$$

$$D_y^{\pm} = 2z \arctan \left[\frac{w/2 \pm y}{z} \right] + (w/2 \pm y) \ln \left[(w/2 \pm y)^2 + z^2 \right], \quad (\text{S10})$$

$$U_z^{\pm} = 2(w/2 \pm y) \arctan \left[\frac{z+d}{w/2 \pm y} \right] + (z+d) \ln \left[(w/2 \pm y)^2 + (z+d)^2 \right], \quad (\text{S11})$$

$$D_z^{\pm} = 2(w/2 \pm y) \arctan \left[\frac{z}{w/2 \pm y} \right] + z \ln \left[(w/2 \pm y)^2 + z^2 \right], \quad (\text{S12})$$

with z being the height above the surface of the Pt line.

Figure S7a shows the Oersted field calculated according to Eq. S8-S12 for a current density of $1 \cdot 10^8$ A/cm² flowing through the Pt layer, at $z = 0.5$ nm above the Pt surface. The y -component $B_y^{Oe} = -3$ mT is approximately constant over the dot surface and directed against B^{FL} . The largest z -component is found at the two extrema of the dots closest to the edge of the Pt line, where $|B_z^{Oe}| = 1.6$ mT. The sign of B_z^{Oe} is opposite on opposite sides of the dot, such that this field can also induce a top/bottom edge asymmetry, supporting the nucleation process induced by B^{FL} , as shown in Figs. S7b and c.

To analyze the role played by the Oersted field and FL torque in the nucleation, we plot in Fig. S7d the θ -components of B^{FL} and B^{Oe} as a function of θ . The fields are evaluated at position (1) in Fig. S6, where the magnetization is tilted by the DMI and external field along $\varphi = 45^\circ$. At this position, the total B_{θ} is positive for all θ , parallel to \mathbf{e}_{θ} (Fig. S2), and thus favours the rotation of the magnetization from up to down. However, without B^{FL} magnetization reversal would not be favoured at this position since B_{θ}^{Oe} is negative over a large range of θ . The opposite argumentation is valid for the magnetization at position (2) in Fig. S6a, where the reversal is favoured by B^{Oe} and hindered by B^{FL} (Fig. S7e). As (1) corresponds to the experimentally observed nucleation, we conclude that B^{FL} is the main cause of the nucleation asymmetry. It is important to note that B_y^{Oe} is approximately constant over the dot area whereas B_z^{Oe} increases rapidly near the Pt line edge. This implies that magnetization nucleation will be eventually also assisted by the Oersted field for Co dots with a diameter comparable to the Pt line width. To demonstrate the effect of B^{Oe} on the switching process, we performed a series of micromagnetic simulations with *i*) $B^{Oe} \neq 0$ and $B^{FL} \neq 0$, *ii*) $B^{Oe} = 0$ and $B^{FL} \neq 0$, *iii*) $B^{Oe} \neq 0$ and $B^{FL} = 0$ and *iv*) $B^{Oe} = 0$ and $B^{FL} = 0$, the results of which are reported in Figs. S7f and g. Without B^{FL} the switching efficiency is strongly reduced, whereas the addition of B^{Oe} to B^{FL} has only a small influence on the reversal mechanism for our device geometry. Note also that the nucleation point moves up along the edge for $B^{FL} = 0$. Additional simulations show that the effect of the Oersted field becomes noticeable when the distance between the edges of the dot and of the Pt current line reduces to less than 50 nm.

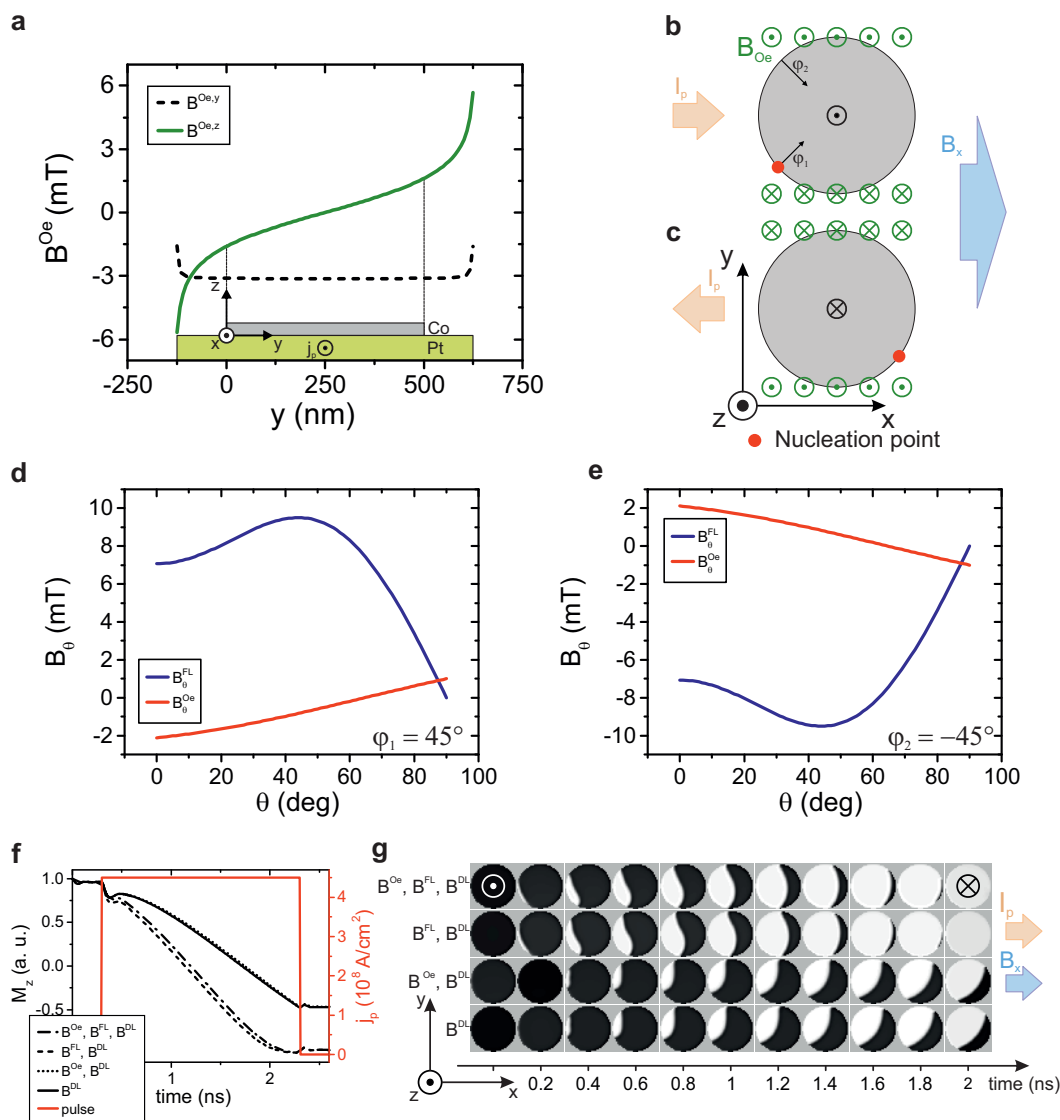


FIG. S7. Influence of the Oersted field on magnetization reversal. **a**, Calculated Oersted field according to Eq. (S8) at a height of 0.5 nm above the Pt line for a positive current pulse of amplitude $1 \cdot 10^8$ A/cm². **b**, Illustration of the nucleation process supported by the z -component of the Oersted field at positive and **c**, negative current. **d**, θ -component of B^{FL} and B^{Oe} as a function of θ during a positive current pulse of amplitude $1 \cdot 10^8$ A/cm² for a spin located at the position (1) and **e**, (2) of the dot (see diagram in Fig. S6). **f**, Simulated time traces for different combinations of B^{Oe} , B^{FL} and B^{DL} . **g**, Corresponding snapshots during the magnetization reversal.

SI 7. SWITCHING OF DEFECTIVE DOTS

All of the measured dots show reproducible switching behavior rather than thermally-induced stochastic reversal, which would result in uniform STXM contrast during the reversal process. However, approximately 50% of the dots showed defect-promoted switching, likely due to inhomogeneities occurred during the patterning process. Such samples are distinguished by the ones presented in the main text by the fact that nucleation always starts from a given point or region rather than alternating between the four dot quadrants. Figure S8 shows a case of defect-promoted switching in which domain nucleation starts at several points around the Co dot edge. Due to the stroboscopic

nature of our measurements, we cannot tell whether the nucleation starts simultaneously at different locations or is randomly distributed over the dot edge. However, we do observe that once a domain has nucleated, the favoured DW propagation direction remains the same (green arrows in Figure S8) and is comparable to the switching behaviour reported in Fig. 3 of the main text. The point at which the reversed domain front collapses (orange dot) is therefore off-centred. Importantly, we find that in all cases the reversal process is robust with respect to the presence of defects, which makes SOT-induced magnetization switching very versatile for applications.

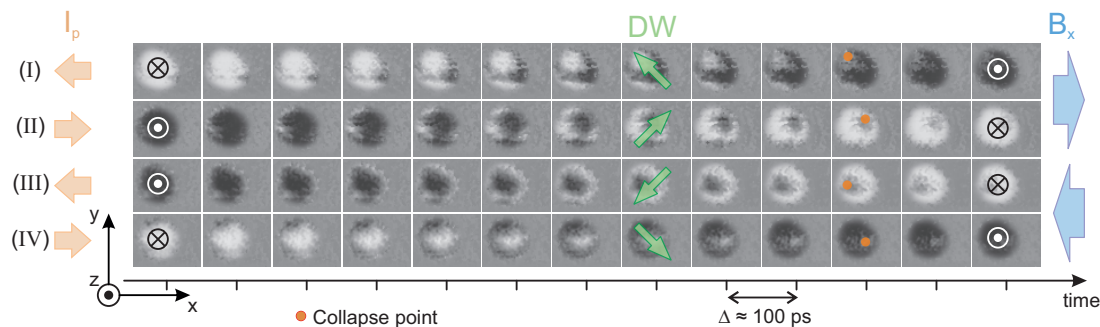


FIG. S8. **Switching in the presence of defects.** Images taken at intervals of 100 ps during the injection of 2 ns long current pulses. DW nucleation is observed at different sites. The point at which the reversed domain front collapses (orange dot) is off-centred, in agreement with the preferential DW propagation direction discussed in the main text (green arrows).

The robustness of SOT-switching relative to the presence of imperfections is confirmed also by micromagnetic simulations of defective dots. Figure S9 compares the switching of an ideal dot with uniform magnetic properties to that of dots with common defects such as regions with reduced magnetic anisotropy or saturation magnetization, as may arise due to the patterning process or thickness fluctuations. For test purposes, some defects are placed on the side of the dot where they would alter the nucleation mechanism described in Sect. SI 5. For such localized edge defects, we observe that a lower magnetization hinders nucleation at the "right" edge of the dot, whereas a lower magnetic anisotropy favors nucleation at the "wrong" edge of the dot, as shown in Fig. S9b and c. In either case, however, we find that nucleation and domain wall propagation from the homogenous regions of the dots proceed almost unimpeded, with only minimal delay relative to the ideal dot. Other defect configurations, such as a continuous edge or a central spot with lower magnetic anisotropy, present more elaborate switching patterns (Fig. S9d and e), similar to those observed in Fig. S8. For all these defects, SOT-induced switching is fast, even though nucleation may start from a defect rather than the ideal edge side.

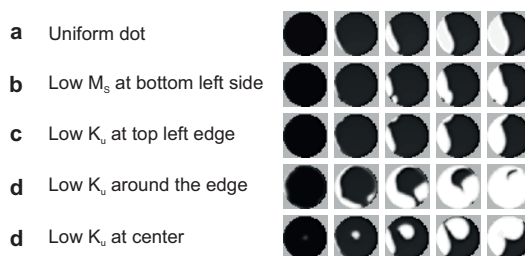


FIG. S9. **Micromagnetic simulations of switching in the presence of defects.** **a**, Snapshots of the magnetic configuration at intervals of 100 ps in the case of a faultless dot. The saturation magnetization is $M_s = 900 \text{ kA/m}$ and the uniaxial anisotropy energy is $K_u = 657 \text{ kJ/m}^3$ (see the Methods Section for a complete list of simulation parameters). **b**, Dot with saturation magnetization reduced to $M_s = 600 \text{ kA/m}$ at the bottom left edge. **c-e**, Dots with magnetic anisotropy energy reduced to $K_u = 550 \text{ kJ/m}^3$ at the top left edge (**c**), entire circumference (**d**), and centre (**e**).

SI 8. COMPARISON BETWEEN FILTERED AND RAW DATA

Given the very low photon count rate at the detector position and the relatively low x-ray absorption contrast corresponding to the 1 nm thick Co layer, the acquisition time of a single sequence of images with 100 ps resolution requires several hours of integration. In order to enhance the magnetic contrast, the intensity of each frame in Fig. 3 of the main text and Fig. S8 has been normalized to the non-magnetic background. Moreover, to improve the signal-to-noise ratio, the intensity of each pixel has been low-pass filtered along the time axis. We have checked that the filtering process does not introduce a significant distortion of the data. For completeness, we compare below the raw and filtered images side-by-side in Figs. S10 and S11. Multi-frame movies constructed from the same series of images are included as separate files in the Supplementary Material.

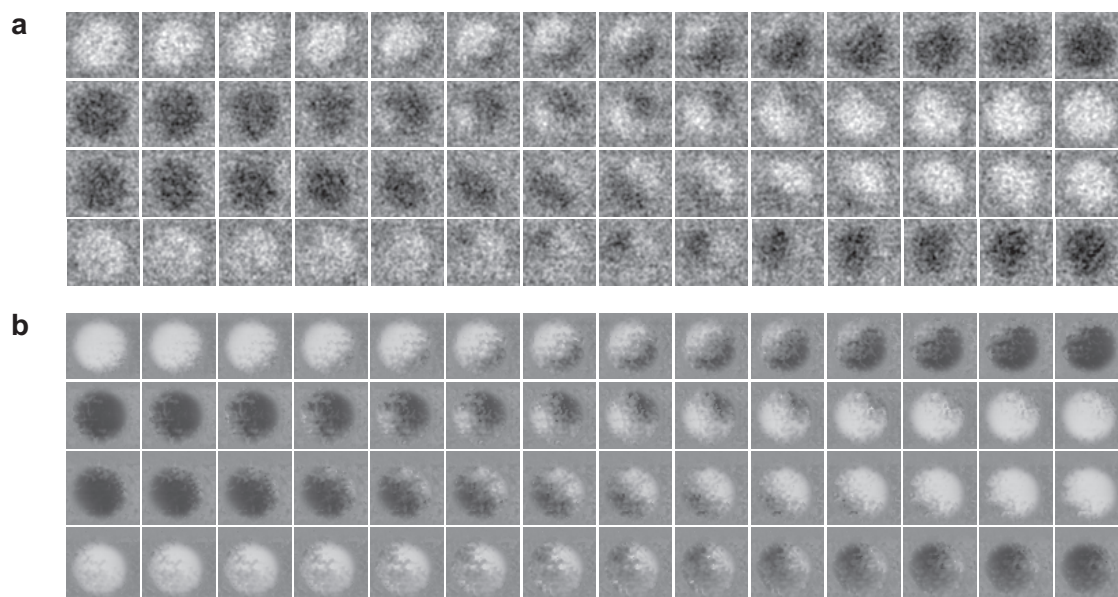


FIG. S10. Comparison of the raw and filtered data shown in Fig. 3. **a**, Raw and **b**, low-pass filtered images.

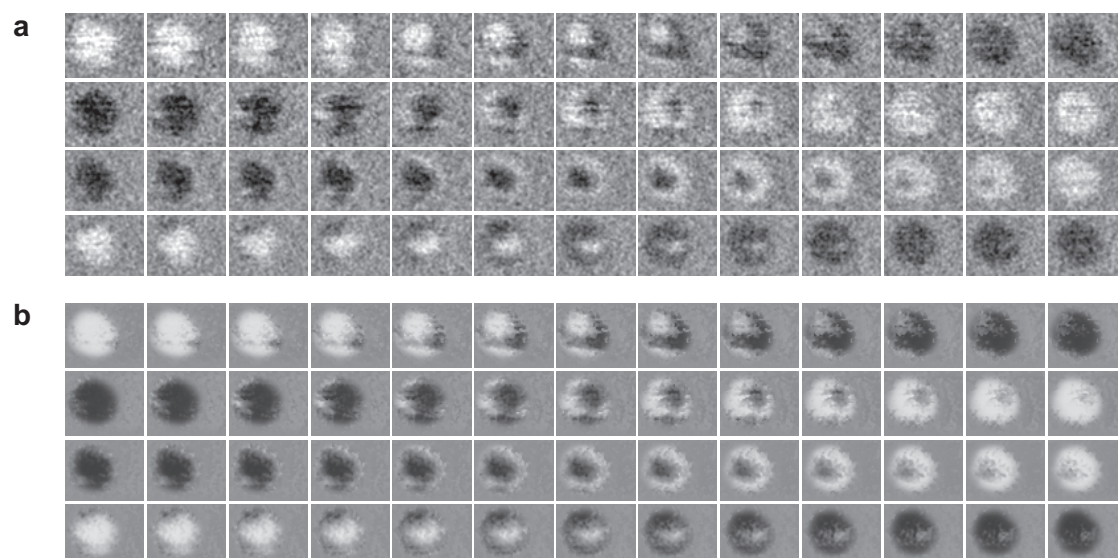


FIG. S11. Comparison of the raw and filtered data shown in Fig. S8. **a**, Raw and **b**, low-pass filtered images.

-
- ¹ Garello, K. *et al.* Ultrafast magnetization switching by spin-orbit torques. *Appl. Phys. Lett.* **105**, 212402 (2014).
 - ² Garello, K. *et al.* Symmetry and magnitude of spin-orbit torques in ferromagnetic heterostructures. *Nature Nanotech.* **8**, 587–93 (2013).
 - ³ Kim, J. *et al.* Layer thickness dependence of the current-induced effective field vector in Ta|CoFeB|MgO. *Nat. Mater.* **12**, 240–5 (2013).
 - ⁴ Avci, C. O. *et al.* Interplay of spin-orbit torque and thermoelectric effects in ferromagnet/normal-metal bilayers. *Phys. Rev. B* **90**, 224427 (2014).
 - ⁵ Mikuszeit, N. *et al.* Spin-orbit torque driven chiral magnetization reversal in ultrathin nanostructures. *Phys. Rev. B* **92**, 144424 (2015).
 - ⁶ Hayashi, M., Kim, J., Yamanouchi, M., & Ohno, H. Quantitative characterization of the spin-orbit torque using harmonic Hall voltage measurements. *Phys. Rev. B* **89**, 144425 (2014).